Check for updates

RESEARCH ARTICLE OPEN ACCESS

Tunable Porosity and Structural Properties of Carbon Aerogels: Adapting Packing Density and Morphology of Dry-Film Cathodes

Magdalena Fiedler[1,2] | Jessica Kröner[3] | Hasti Rahimi[1,2] | Marina Schwan[3] | Barbara Milow[3,4] | Felix Hippauf[1] | Susanne Dörfler[1] | Stefan Kaskel[1,2]

[1]Fraunhofer Institute for Material and Beam Technology IWS, Dresden, Germany | [2]Chair of Inorganic Chemistry 1, Faculty of Chemistry and Food Chemistry, TU Dresden, University of Technology, Dresden, Germany | [3]Linder Höhe, Deutsches Zentrum für Luft- und Raumfahrt e.V., Köln, Germany | [4]Universität zu Köln, Greinstraße, Köln

Correspondence: Susanne Dörfler (susanne.doerfler@iws.fraunhofer.de)

Received: 13 January 2026 | **Revised:** 27 May 2026 | **Accepted:** 10 June 2026

Keywords: all-solid-state batteries | argyrodite | carbon aerogel | dryfilm | lithium-sulfur batteries | packing-density

ABSTRACT

The increasing demand for high-energy-density storage systems to support green energy technologies has highlighted the limitations of lithium-ion batteries and spurred interest in lithium-sulfur solid-state batteries (LS-SSBs), as they offer significant advantages, such as high theoretical energy densities and improved safety. Despite intense research in the recent years, there is a lack of understanding regarding a favorable carbon structure as a sulfur host in LS-SSBs. This study investigates the use of carbon aerogels (CAs) with adaptable porosity and mechanical properties as conductive matrices in LS-SSB cathodes. Two different CAs are examined: a brittle, mesoporous aerogel (p-CA) and a flexible, macro- and microporous aerogel (f-CA). High sulfur utilization (~1500 mAh g_S^{-1}) is achieved using p-CA, but it suffers from low Coulombic efficiency and reversibility. Conversely, f-CA exhibits lower sulfur utilization but improved cycling stability. The combination of both aerogels results in a higher packing density of the LS-SSB cathode. High sulfur utilization and enhanced long-term stability are realized for the mixed cathode. These results demonstrate the potential of CAs as a customizable, scalable host matrix for LS-SSBs, enabling improved cathode morphology and electrochemical performance through controlled tuning of their structural and mechanical properties.

1 | Introduction

Due to the increasing demand for green energy, high-energy-density storage solutions are essential to ensure a reliable and sufficient energy supply. However, lithium-ion batteries, which represents the state-of-the-art, face their theoretical energy density limits (300 Wh kg^{-1}) [1, 2]. Lithium-sulfur batteries (LSBs) are among the most promising candidates to tackle these challenges and enable high energy densities. LSBs exhibit a high theoretical energy density (2500 Wh kg^{-1}), enabled by the metallic lithium anode and sulfur as cathode material [3, 4]. Both elements are characterized by a high specific capacity (3860 mAh g_{Li}^{-1} and 1672 mAh g_S^{-1}) and low densities (0.53 and 2.06 g cm^3), which is why high energy densities are expected for LSBs [4–7]. Despite intensive research over the past decades, LSBs with liquid electrolyte still face major challenges such as polysulfide-shuttle (PS-shuttle) and dendrite formation, limiting the energy densities under real conditions and during long-term cycling [8].

Lithium-sulfur solid-state batteries (LS-SSBs) are envisaged to tackle these problems and to overcome the limitations of LSBs. The use of a solid electrolyte (SE) brings several advantages

Magdalena Fiedler and Jessica Kröner contributed equally to this study.

This is an open access article under the terms of the Creative Commons Attribution License, which permits use, distribution and reproduction in any medium, provided the original work is properly cited.

© 2026 The Author(s). *Batteries & Supercaps* published by Wiley-VCH GmbH.

as it suppresses dendrite formation and inhibits the PS-shuttle completely due to its Li^+-ion selectivity. Furthermore, it enables a low electrolyte: sulfur mass ratio and enhances safety due to of the noncombustibility of SEs [9, 10].

However, the design of LS-SSBs needs further investigation and optimization to enable the theoretical energy densities. One major challenge is the design of the cathode composite. Sulfur, which is an insulator, needs to be encapsulated within an electronically conducting matrix (e.g., carbon) to enable the electrochemical conversion. Additionally, ionic pathways within the cathode composite need to be ensured as electrochemical reactions occur at the triple-phase boundaries and transport limitations at these interfaces can hinder ion mobility and reduce sulfur utilization [11–13]. High-energy ball milling (HBM) is the most commonly used method for preparing cathode composites in LS-SSBs, as it ensures a homogeneous mixture and promotes the formation of well-connected three-phase boundaries. However, this method requires several hours of high rotational speed (>400 rpm), subjecting active material, carbon (C), and the SE to intense mechanical forces. As a result, the particle morphology is significantly altered, making it difficult to investigate the specific influence of different carbon structures [13–15]. Moreover, HBM often leads to composites with low porosity and presents major scalability challenges due to long processing times and its inherently batch-wise nature [16]. In contrast, low-energy ball milling (LBM), performed at reduced speed and time (300 rpm for 15 min), has demonstrated that the carbon's structure can be maintained. Despite the lower mechanical impact, LBM still enables comparable electrochemical performance while maintaining the porous structure of the carbon [14, 16, 17]. Notably, the best-performing mesoporous carbon to date, C-Novel by Toyo Tanso Co., Ltd., has demonstrated superior sulfur utilization and excellent retention of discharge capacity over extended cycling. However, it is relatively cost-intensive, as its pore structure is created using a nanoparticle-based templating approach, which inherently limits the overall carbon yield [16, 17]. More importantly, LBM significantly reduces mechanical stress during mixing, making it a more scalable and energy-efficient approach. It also opens new opportunities for cathode design and enhanced sulfur utilization, particularly when using micro- or mesoporous carbon materials [14, 16]. A careful design and balancing of the cathode components, sulfur, carbon, and sulfide-based SE, is needed to ensure the sulfur conversion. During the conversion of S_8 to Li_2S, a significant volume expansion is presumed, since the density of Li_2S is lower ($1.66\,g\,cm^3$) compared to S_8 [18]. The volume change during cycling poses an additional challenge, as mechanical stress is excerted on the cathode, potentially resulting in contact loss or crack formation. Consequently, the cathode's design in LS-SSBs has moved into the focus of researchers to enable the full conversion of sulfur and buffer the volume change during cycling. One possibility is to adapt the carbon, which is used as host material for sulfur. Several studies demonstrated that high sulfur utilization is enabled using different carbons with differing structure and porosity, such as carbon nanofibers, carbon nanotubes, mesoporous carbons, or hierarchical carbons [16, 17, 19–23]. However, there is still a lack of understanding of which carbon structure is favorable to ensure high sulfur utilization, rate stability and long-term stability of LS-SSBs, especially when using the harsh conditions of HBM for preparing the cathode composite, the structure of the carbon host is likely destroyed [17]. In this context, 3D carbon aerogels (CAs) offer a distinct advantage due to their exceptionally high surface area and inherent electrical conductivity, making them particularly attractive for energy storage applications [24]. Their effectiveness has already been demonstrated in previous studies on Li–S batteries [25–27]. Moreover, CAs provide a high degree of structural tunability, especially in terms of pore size distribution and total pore volume, which can be precisely adjusted to meet specific requirements. Importantly, their mechanical properties such as compressibility, fragility, elasticity, and softness can also be tailored according to application needs [28]. These mechanical characteristics are not only important in the end application but also play a significant role in the preparation and processing of the material, such as grinding and mixing. Brittle and flexible materials behave differently under high pressures that are usually applied in LS-SSBs, and their microstructure can be altered differently depending on their properties. In particular, the energy input during pulverization should not be underestimated, as it can irreversibly change the microstructure of flexible or brittle aerogels [29].

In this work, to deepen the understanding of the influence of pore size and mechanical stability of the carbon on the electrochemical sulfur cathode performance in combination with argyrodite SE, CAs have been used as a conductive matrix. Our previous work demonstrated the influence of the carbon structure on the electrochemical performance [16]. It was assumed that the transport of Li^+-ions towards the reactive sites was blocked in micropores, whiler this behavior was not found in LS-SSB cathodes with mesoporous carbon. A higher average pore size of the carbon resulted in higher sulfur utilization. It was also assumed that the mechanical stability of the carbon particles influenced the cathode's morphology. To further investigate these effects, we conducted a study using different sulfur loadings with two types of CAs (flexible and brittle) and their combinations. The resulting electrochemical, mechanical, and morphological analyses presented in this work aim to provide insights into the role of carbon structure and support the development of an optimized cathode composite for LS-SSBs.

2 | Results and Discussion

2.1 | Material Characterization

2.1.1 | Synthesis and Properties of Carbon Aerogels with Different Mechanical Properties

Two aerogels were synthesized for the study: p-CA represents a brittle aerogel [30] and f-CA an elastically deformable—so-called flexible aerogel [31]. First, two different organic resorcinol-formaldehyde aerogels (RF) were produced in a sol–gel process, dried in supercritical carbon dioxide and then converted to CAs, but only one CA was activated with CO_2 (f-CA). Both CAs differ in their density, microstructure, electrical conductivity, and compression behavior.

Figure 1A shows the microstructure of a p-CA. The microstructure consists of a dense network and small secondary particles in the range of 20–50 nm, whereas the network of f-CA consists of significantly larger secondary particles in the range of 100–200 nm and large pores between the particles (Figure 1B). This

25666223, 2026, 7, Downloaded from https://chemistry-europe.onlinelibrary.wiley.com/doi/10.1002/batt.70384 by Fraunhofer IRB, Wiley Online Library on [05/08/2026]. See the Terms and Conditions (https://onlinelibrary.wiley.com/terms-and-conditions) on Wiley Online Library for rules of use; OA articles are governed by the applicable Creative Commons License

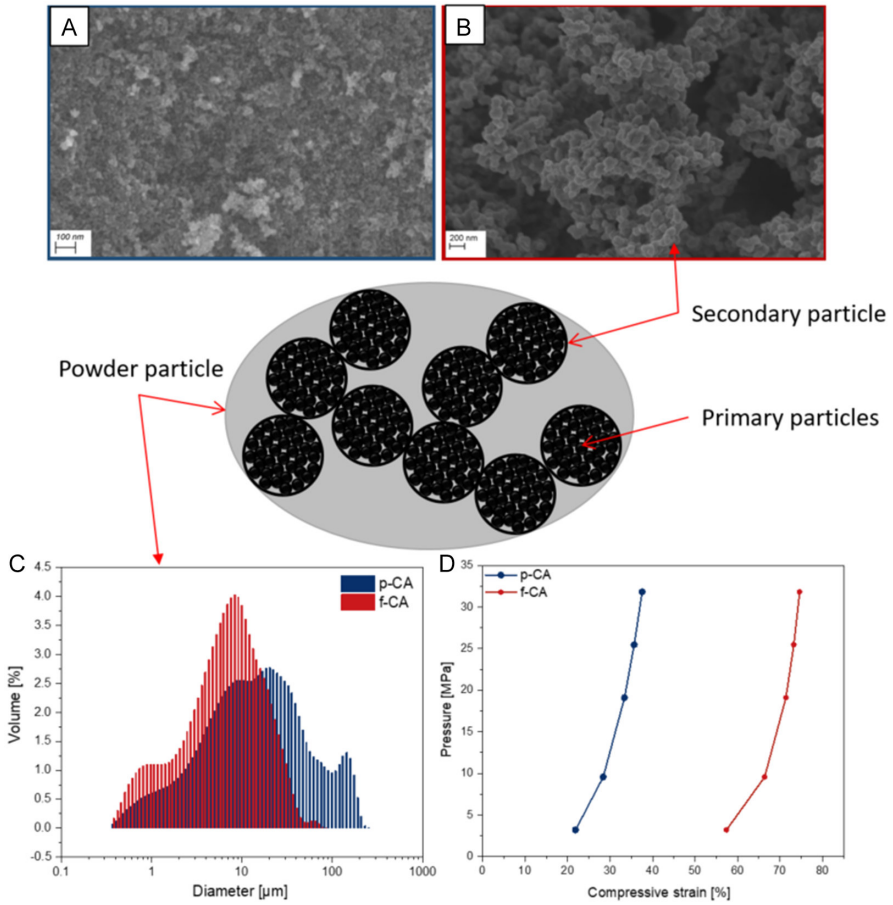

FIGURE 1 | (A) p-CA with small secondary particles of about 20–50 nm, (B) Microstructure of monolithic f-CA with secondary particles of about 100–200 nm, (C) Powdered particle size distribution of carbon aerogels, (D) compression behavior of pulverized carbon aerogels; Center: Schematic visualization of different particles size definitions.

somewhat loose structure of f-CA is decisive for its compression behavior. During compression, the pore walls have sufficient space to deform reversibly to a certain degree without breaking. The structure of p-CA has a denser network so that it cannot be compressed as much as f-CA.

Figure 1C shows the powdered particle size distribution of both aerogels. Particles here refer to the powder granule particle size and not, as described above, the network particle size (primary or secondary). The p-CA shows a bimodal distribution with peaks at about 50 and 180 µm. In contrast, f-CA exhibits a very narrow distribution with powdered particles of 20 µm. Both aerogels synthesized as monolithic structures were ground with the same milling parameters. However, they exhibited different particle sizes after milling. This is due to the fact that these two CAs have different microstructures and properties. Presumably, this milling energy input is sufficient for the flexible f-CA to be finely milled, whereas it is not sufficient for the harder p-CA to reach the same particle sizes.

The fact that both aerogels have different compression behavior is confirmed by the findings shown in Figure 1D. Here, compression is plotted against pressure. The first measurement point was recorded at 3.6 MPa. To achieve this pressure, p-CA was be compressed by 22%. A completely different behavior is shown by f-CA. Here the compression is almost three times higher with 57% reduction at the same pressure. The courses of the curves are very similar, the slope is slightly steeper for p-CA. The compression increases with higher pressure, the powder is highly compacted. At 31.8 MPa, p-CA reaches the maximum value of 35.9% and f-CA 79.1%. This illustrates that f-CA can be compressed twice as much as p-CA.

Table 1 below shows the general properties of both aerogels. The values given in the table illustrate once more how different

TABLE 1 | General properties of carbon aerogels.

Properties	p-CA	f-CA
Envelope density, g cm^{-3}	0.57	0.07
Skeletal density, g cm^{-3}	2.08	2.71
Porosity, %	73	97
Specific surface area, m^2 g^{-1}	693	836
Micropore volume, cm^3 g^{-1}	0.10	0.31
Mesopore volume, cm^3 g^{-1}	0.85	0.07
Average primary particle size, nm[a]	4.2	2.7
Compressive strain at 1 kN, %	22	57
Electrical conductivity at 1 kN, mS cm^{-1}	2940	1830

[a]Calculated with equation from [26].

25666223, 2026, 7, Downloaded from https://chemistry-europe.onlinelibrary.wiley.com/doi/10.1002/batt.70384 by Fraunhofer IRB, Wiley Online Library on [05/08/2026]. See the Terms and Conditions (https://onlinelibrary.wiley.com/terms-and-conditions) on Wiley Online Library for rules of use; OA articles are governed by the applicable Creative Commons License

both aerogels are. The f-CA has an eight times lower envelope density than p-CA and due to this also a significantly higher porosity of 97%, which primarily results from the presence of macropores. Although the SEM images show that f-CA consists of larger particles, f-CA has higher specific surface area. However, if the size of the primary particles is calculated (from Brunauer-Emmett-Teller (BET) results [32]), one can identify a different trend. The calculation shows that p-CA has primary particles twice as large (4.2 nm) as f-CA (2.7 nm). This explains why the surface area of f-CA is higher ($836\,m^2g^{-1}$) than that of p-CA ($693\,m^2\,g^{-1}$). These primary particles then form much larger particles (secondary particles), which are visible in the SEM.

A ball milling routine with lowered energy impact, LBM, was used to prepare the LS-SSB cathodes. To investigate the influence of ball milling on the carbon structure, physisorption measurements have been carried out before (Figure 2) and after ball milling (Figure 3) with the same parameters, but without adding sulfur and argyrodite SE. The brittle CA (p-CA) displays the majority of pore volume in a range of pore sizes between 3 and 20 nm, consistent with a mesoporous structure (Figure 2B). According to IUPAC, p-CA exhibits the isotherm type IV with a hysteresis loop H1, which is typical for materials with a narrow range of uniform mesopores [33]. In contrast to that, here only micropores in this range can be observed for the flexible carbon f-CA, where the majority of pores are present below a size of 1 nm. The flexible CA shows a type I isotherm, which is characteristic for narrow micropores. The sum of meso- and micropore volume of p-CA is $0.95\,cm^3\,g^{-1}$, while a lower pore volume of $0.38\,cm^3\,g^{-1}$ is detected for f-CA. Macropore volume is undetectable by N_2 adsorption at 77 K, but the exact value can be calculated using the envelope density and skeleton density from Table 1, which shows that the total pore volume of pristine f-CA is $13.91\,cm^3\,g^{-1}$, of which $13.53\,cm^3\,g^{-1}$ corresponds to macropores. In comparison, in pristine p-CA, the total pore volume is $1.27\,cm^3\,g^{-1}$, leaving only $0.32\,cm^3\,g^{-1}$ for macropores. The specific surface area (SSA) of p-CA is $693\,m^2\,g^{-1}$ and $836\,m^2\,g^{-1}$ for f-CA. Hg-intrusion was carried out (Figure 2C), too, even though the resulting curves should not be over-interpreted, especially for the flexible carbon aerogel f-CA. It is known from literature [34, 35] that, under the tremendously high pressures during Hg-intrusion (around 400 MPa), flexible materials and their porosity are altered, thereby falsifying the resulting values, as deformation of the pores may distort the measurements, whereas stiffer frameworks withstand the pressure and allow for more accurate mercury penetration. Nevertheless, it can be seen that, for p-CA mesopores at a pore width of 10 nm are visible both via nitrogen physisorption as well as mercury intrusion. For f-CA, the majority of pore volume stems from large macropores that are only visible during mercury intrusion. It should be noted that the absolute value of pore width might be altered due to the compression of the sample during the intrusion, a broad pore size distribution can be observed. For f-CA, the absolute value of the pore volume of $9.53\,cm^3\,g^{-1}$ (based on mercury intrusion) differs more from the value that was estimated from tapped density ($13.91\,cm^3\,g^{-1}$). For p-CA, however, the value differs less: $1.27\,cm^3\,g^{-1}$ calculated from tap density and 1.95 from mercury intrusion.

The isotherms after ball milling of the pure CAs are displayed in Figure 3A, where no significant difference was observed. p-CA

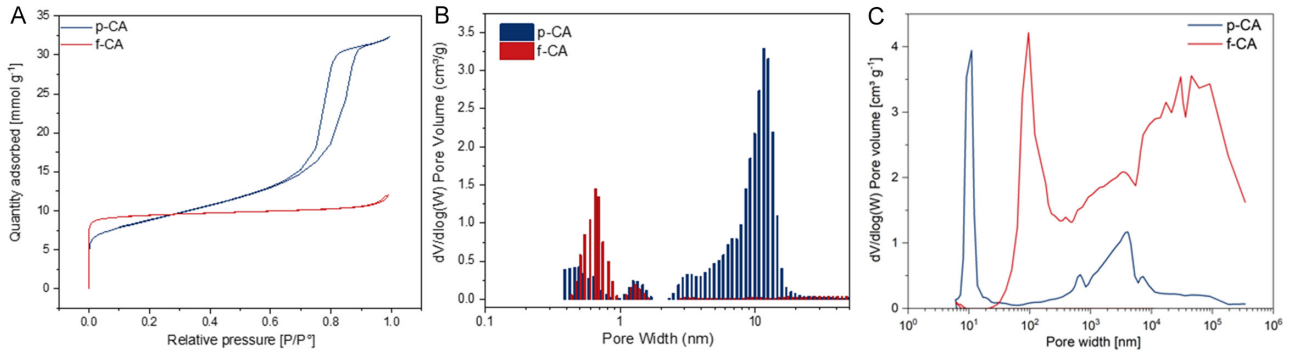

FIGURE 2 | (A) Isotherms of both carbon aerogels (77 K, N_2), (B) pore size distributions of p-CA and f-CA calculated with DFT, (C) pore size distributions of p-CA and f-CA calculated with mercury intrusion porosimetry (MIP).

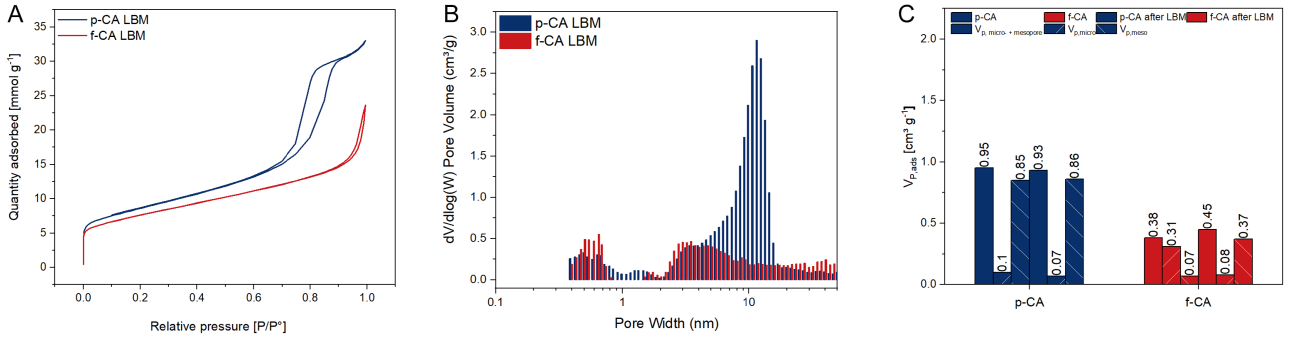

FIGURE 3 | (A) Isotherms of both carbon aerogels (77 K, N_2) after ball milling, (B) Pore size distribution after ball milling and (C) detailed porosity before and after ball milling of the used carbon aerogels.

25666223, 2026, 7, Downloaded from https://chemistry-europe.onlinelibrary.wiley.com/doi/10.1002/batt.70384 by Fraunhofer IRB, Wiley Online Library on [05/08/2026]. See the Terms and Conditions (https://onlinelibrary.wiley.com/terms-and-conditions) on Wiley Online Library for rules of use; OA articles are governed by the applicable Creative Commons License

displays a comparable isotherm and consequently, a comparable pore size distribution, where the micro- and mesopore volumes are only slightly affected. The mesopore volume is nearly constant, namely 0.85 $cm^3\ g^{-1}$ before and 0.86 $cm^3\ g^{-1}$ after LBM, while the micropore volume is reduced from 0.10 to 0.07 $cm^3\ g^{-1}$. In contrast to that, a change in pore size distribution was observed for f-CA, as shown in Figure 3B. The amount of pores in below 1 nm is reduced, and the micropore volume decreases from 0.31 to 0.08 $cm^3\ g^{-1}$. Additionally, an increased mesopore volume of 0.37 $cm^3\ g^{-1}$ was detected after LBM, compared to 0.07 $cm^3\ g^{-1}$ before ball milling. During LBM, the thinner microporous walls of f-CA are more prone to fracture, causing some micropores to collapse and merge into mesopores, whereas the architecture of p-CA remains essentially unchanged. The slight increase in the combined micro- and mesopore volume of f-CA after LBM can be explained by its macroporosity. After LBM, the micro- and mesopore volume increases slightly to 0.45 $cm^3 g^{-1}$, confirming that the macroporous framework, which changes from 13.91 to 13.86 $cm^3 g^{-1}$, remains largely intact under these conditions. In general, a certain porosity within the carbon structure was maintained after LBM. Both CAs, which demonstrated different mechanical properties, were affected in a different manner by LBM. This leads to the assumption that the different mechanical properties accompanied by different porosities and particle sizes result in different electrochemical behavior, which needs to be further discussed.

2.2 | Characterization of LS-SSB Cathodes

2.2.1 | Electrochemical Performance of LS-SSB Cathodes

Both materials have been investigated as a conductive material in LS-SSB cathodes. Therefore, sulfur was melt-infiltrated into the carbon structure. Three different sulfur ratios within the carbon/sulfur (C/S)-composite were used. A sulfur content of 60 wt% was used to compare with recent results in the literature and in our previous work [16, 36]. Additionally, the sulfur content was adapted based on the micro- and mesopore volume of the carbon before ball milling. The adaptation of sulfur content is intented to ensure the homogeneous distribution within the carbon porosity, thereby promoting good electrical conductivity towards the reactive sites. The specific sulfur ratios have been calculated according to the following Equation (1), where V represents volume, m is mass, ρ indicates density, and ω stands for weight percent

$$V_S = V_{pore,C} \tag{1a}$$

$$m_S = V_{pore.C} \cdot m_C \cdot \rho_S \tag{1b}$$

$$m_S = V_{pore,C} \cdot 1g \cdot 2.06\ g\ cm^{-3} \tag{1c}$$

$$\omega_S = \frac{m_S}{m_S + m_C} \tag{1d}$$

As discussed in the introduction, the conversion of sulfur to lithium sulfide is accompanied by a high volume increase during reduction to Li_2S. In this process, the volume increases by 74%. The volume change of the cathode active material is expected to cause mechanical stress within the cathode, potentially resulting in contact losses and degradation mechanisms during cycling. Consequently, the sulfur content was reduced based on to the amount of Li_2S that can be buffered by the pore volume of the CAs at 100% of sulfur utilization during cycling. The sulfur volume based on the theoretical Li_2S volume has been determined according to Equation (2)

$$V_{Li2S} = V_{pore,C} \tag{2a}$$

$$m_{Li2S} = V_{pore.C} \cdot m_C \cdot \rho_{Li2S} \tag{2b}$$

$$m_{Li2S} = V_{pore,C} \cdot 1\ \ g \cdot 1.66\ \ g\ cm^{-3} \tag{2c}$$

$$m_S = \frac{m_{Li2S}}{M_{Li2S}} \cdot \frac{1\ mol_S}{1\ mol_{Li2S}} . M_S \tag{2d}$$

$$m_S = \frac{m_{Li2S}}{45.95 \frac{g}{mol}} \cdot 32.06 \frac{g}{mol} \tag{2e}$$

$$\omega_S = \frac{m_S}{m_S + m_C} \tag{2f}$$

Both CAs were investigated with the corresponding sulfur ratios. The as-prepared C-S-composites were mixed with Li_6PS_5Cl as sulfide-based SE in weight ratio of 1:1 to prepare the LS-SSB cathodes. The electrochemical performance of the cathode containing p-CA is demonstrated in Figure 4. The variation of sulfur content resulted in different electrochemical behavior. At 53% ($V_{Li2S} = V_{micro-+mesopore}$) and 60% sulfur (standard amount) within the composite, the cathodes demonstrate almost comparable electrochemical performance. In contrast to that, a significantly lower addressability of sulfur was observed when increasing the sulfur content to 65% ($V_S = V_{micro-+mesopore}$).

The voltage profiles of the tested cathodes at different C-rates demonstrate one voltage plateau during both, charging and discharging (Figure 4A–C), as expected in LS-SSBs. It should be noted that shoulders are observed during discharge, which can be interpreted as a stepwise conversion of sulfur to lithium sulfide. However, this process is not yet fully understood yet in the literature. It was observed that the voltage hysteresis increases with increasing sulfur content, which can be attributed to rising overpotentials during cycling. These can be explained by kinetic limitations during cycling.

As illustrated in Figure 4D, the cathodes containing 53% sulfur within the composite (circle) and 60% sulfur (square) exhibit high initial discharge capacities above 1300 mAh g_s^{-1}. An increase in discharge capacity during the first cycles can be observed, reaching 1450 mAh g_s^{-1} (60% sulfur) and 1350 mAh g_s^{-1} after the formation cycles. Increasing the C-rates results in reduced discharge capacities, where capacities below 400 mAh g_s^{-1} are observed at 0.5C. Following the C-rate test, 40 cycles at 0.1C were performed in order to gain insights into long-term performance of the LS-SSB cathodes. Both cathodes display a linear capacity degradation. The cathode containing 53% sulfur within the composite demonstrates a discharge capacity of 1120 mAh g_s^{-1} in cycle 13. After 50 cycles, a discharge capacity of 360 mAh g_s^{-1} is obtained. The cathode containing 60% sulfur demonstrates 1230 mAh g_s^{-1}

25666223, 2026, 7, Downloaded from https://chemistry-europe.onlinelibrary.wiley.com/doi/10.1002/batt.70384 by Fraunhofer IRB, Wiley Online Library on [05/08/2026]. See the Terms and Conditions (https://onlinelibrary.wiley.com/terms-and-conditions) on Wiley Online Library for rules of use; OA articles are governed by the applicable Creative Commons License

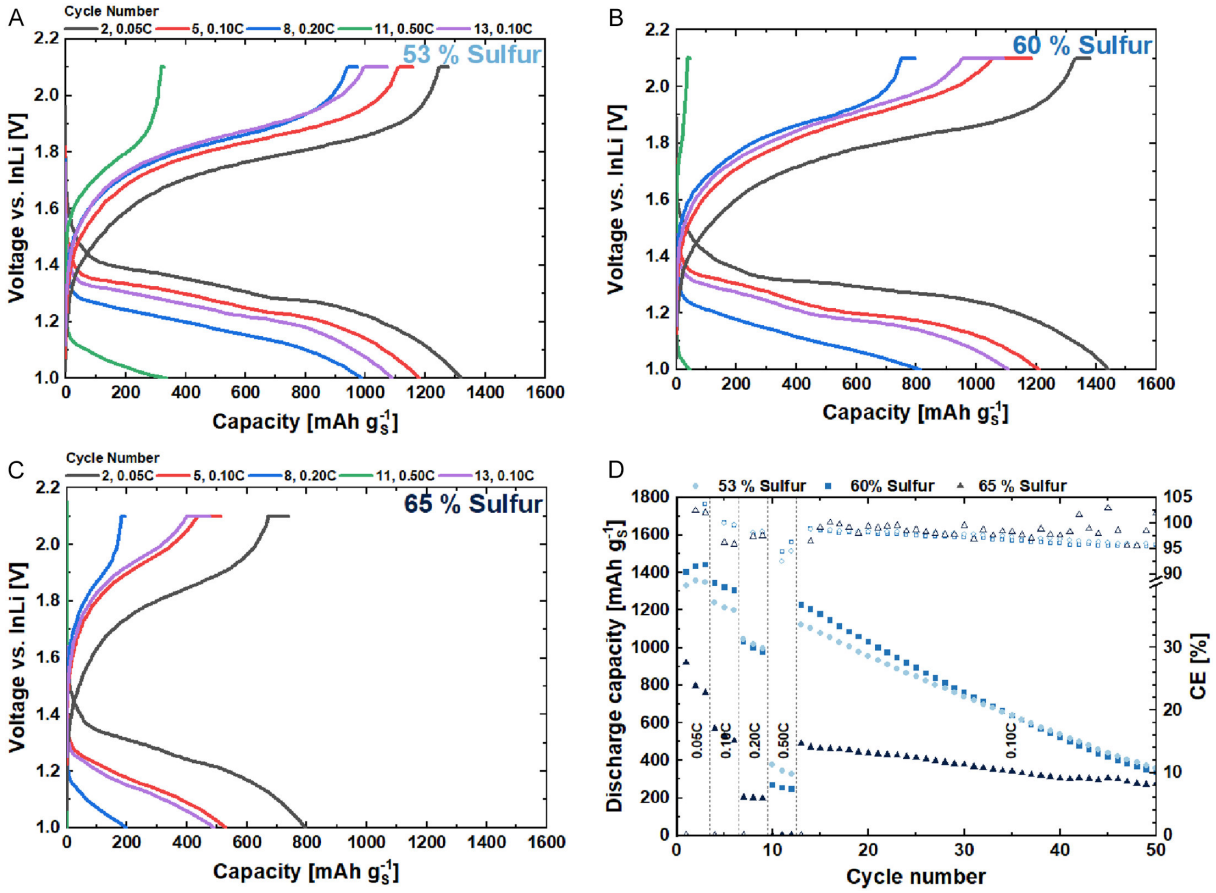

FIGURE 4 | Electrochemical performance of p-CA at 25°C with (A–C) voltage profiles at different C-rates of the cathodes with varied sulfur content within the C-S-composite, (D) capacity retention of the evaluated LS-SSB cathodes with varied sulfur content.

after 13 cycles. The discharge capacity is decreased to 360 mAh g_s^{-1} in cycle 50. A lower sulfur utilization is noticeable for the cathode containing 65% sulfur (triangle). An initial discharge capacity of 1100 mAh g_s^{-1} is observed, which decreases in the subsequent cycles. The sulfur utilization is strongly affected by increasing C-rates, approaching zero at the highest C-rate. During long-term cycling, a discharge capacity of 590 mAh g_s^{-1} is observed in cycle 13, which is subsequently decreased to 280 mAh g_s^{-1} in cycle 50.

It is assumed that, in the case of the 65 wt% cathode, the sulfur fully occupies the mesopore and micropore volume of the p-CA. This pore-filling effect results in kinetic limitations during the sulfur conversion. Furthermore, it is assumed that mechanical stress within the cathode increases, as no porosity within the carbon structure is left to buffer the volume expansion during the conversion of sulfur to lithium sulfide.

Across the p-CA cathodes, Coulombic efficiency (CE) of ~95% is consistent with with capacity fading, which could be attributed to the large mesoporous interfacial area promoting parasitic cathode–electrolyte reactions despite the initially high sulfur utilization.

In contrast to mesoporous p-CA, f-CA is predominantly macroporous but also contains a significant fraction of micropores, which play a critical role in its electrochemical behavior. Again, three different sulfur contents are used, namely 31% ($V_{\text{micro-+mesopore}} = V_{Li2S}$) and 44% ($V_{\text{micro-+mesopore}} = V_S$) alongside the standard sulfur amount of 60% (Figure 5). When comparing the voltage profiles at different C-rates (Figure 5A–C) it can be seen that the voltage plateau is less pronounced with increasing sulfur content. Even at the lowest sulfur content of 31% (Figure 5A), a sloping voltage profile is observed. This effect is pronounced more pronounced at increased sulfur contents.

The three cathodes show distinct differences in sulfur utilization. As shown in Figure 5D, at the lowest sulfur content of 31%, a high initial discharge capacity of 1240 mAh g_S^{-1} was observed. The discharge capacity was as low as ≈600 mAh g_S^{-1} in the subsequent cycles at 0.05C. The capacity is further decreased at increasing C-rates, displaying 500 mAh g_S^{-1} at 0.1C, 350 mAh g_S^{-1} at 0.2C, and 80 mAh g_S^{-1} at the highest C-rate of 0.5C. Decreasing the C-rate to 0.1C resulted in a discharge capacity of 510 mAh g_S^{-1} in cycle 13. A high CE of 99.8% is observed during long-term cycling, resulting in low capacity fading. In cycle 50, 385 mAh g_S^{-1} is obtained, demonstrating 77% of the discharge capacity compared to cycle 5 (at the same C-rate). Thus, high capacity retention was achieved for the lowest sulfur content. The loss of capacity after the first discharge can be attributed to limitations of the Li^+-ion transport in micropores. Increasing the sulfur content within the composite results in a reduced sulfur utilization. At 44% sulfur content, a discharge capacity of 590 mAh g_S^{-1} is observed during the first cycles that drops to 345 mAh g_S^{-1} in cycle 2 as well as during long-term cycling. The standard sulfur content of 60% demonstrates poor electrochemical performance, with only 100 mAh g_S^{-1} during the first cycles as well as during long-term performance. Considering

25666223, 2026, 7, Downloaded from https://chemistry-europe.onlinelibrary.wiley.com/doi/10.1002/batt.70384 by Fraunhofer IRB, Wiley Online Library on [05/08/2026]. See the Terms and Conditions (https://onlinelibrary.wiley.com/terms-and-conditions) on Wiley Online Library for rules of use; OA articles are governed by the applicable Creative Commons License

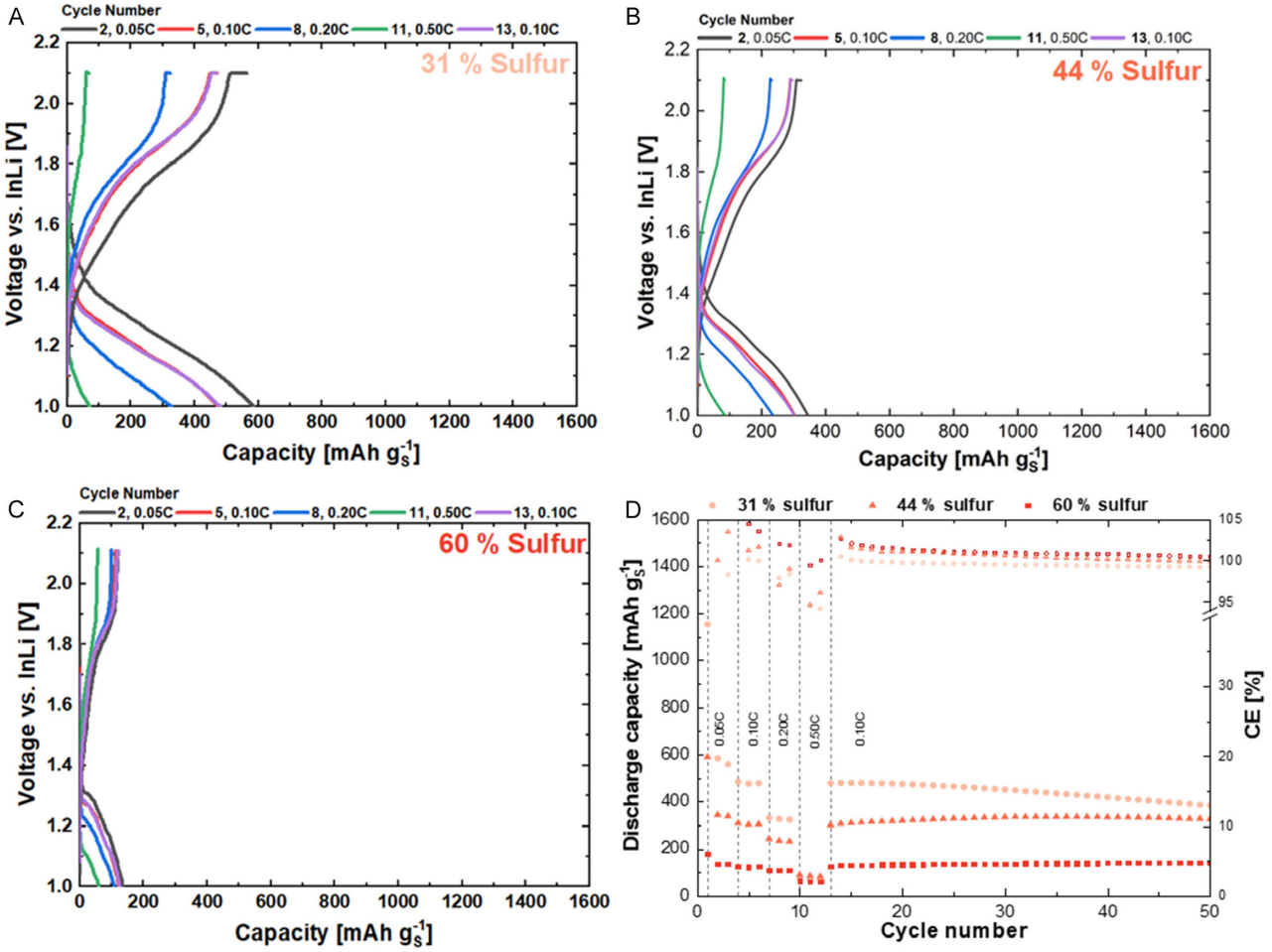

FIGURE 5 | Electrochemical performance of the f-CA with (A–C) voltage profiles at different C-rates of the cathodes with varied sulfur content within the C-S-composite, (D) capacity retention of the tested LS-SSB cathodes with varied sulfur content.

that 60 wt% loading exceeds the combined micro- and mesopore volume, these findings suggest that the macropores are neither accessible nor sufficiently interconnected to host sulfur in f-CA.

Both CAs displayed differing electrochemical performance. The mesoporous carbon p-CA demonstrated high sulfur utilization and distinct voltage plateaus, as expected in LS-SSBs. However, the CE was rather low, consequently leading to constant capacity fading during long-term cycling. In contrast to that, the f-CA, which is predominantly macroporous but contains micropores that dominate electrochemical behavior exhibited a significantly lower discharge capacity. High overpotentials were observed, resulting in sloping voltage profiles. Additionally, a strong dependence on the sulfur content was observed. The highest sulfur utilization was achieved for the lowest sulfur content of 31% within the composite (15.5% within the cathode), but the energy density on the cathode level is drastically reduced, compared to the p-CA cathodes. However, a high CE was demonstrated for these cathodes, which can be attributed to the limited number of reactive sites in the micropores, possibly improving the long-term performance.

2.2.2 | *Electric Conductivities of CAs and LS-SSB Cathodes*

Electrical conductivities of pure and sulfur infiltrated (Figure S1A) aerogels were measured with increasing pressure from 3.6 to 31.8 MPa. At low pressures, only dislocation of particles takes place, with increasing pressure, as postulated by Euler [37], irreversible particle deformation occurs. Powder compression creates many contacts between the particles, so that electron transport is significantly improved and the electrical conductivity increases with increasing pressure. As expected, due to the higher density [38, 39], the conductivity of p-CA is considerably higher than that of f-CA. The behavior of sulfur-infiltrated aerogels is also predictable. The conductivities of infiltrated samples are lower than those of pure aerogels. This is expected, as sulfur is insulating in nature and its presence in the pores leads to a reduction in conductivity. At higher pressures, a large amount of sulfur is likely pressed out of the pores, and the improved particle-to-particle contact increases the overall conductivity.

Additionally, electric conductivity measurements of the whole cathodes were carried out to receive further insights into the cathode's kinetics (Figure S1B).

p-CA displays electrical conductivities at approximately 100 mS cm^{-1}. Furthermore, no significant trend is observed with respect to the sulfur content. This can be explained by the fact that the sulfur content does not exceed the meso- and micropore volume of the p-CA, leading to the assumption that the sulfur is hosted within the carbon structure after melt-infiltration. Hence, the influence of the insulating sulfur on the electrical conductivity

25666223, 2026, 7, Downloaded from https://chemistry-europe.onlinelibrary.wiley.com/doi/10.1002/batt.70384 by Fraunhofer IRB, Wiley Online Library on [05/08/2026]. See the Terms and Conditions (https://onlinelibrary.wiley.com/terms-and-conditions) on Wiley Online Library for rules of use; OA articles are governed by the applicable Creative Commons License

is less pronounced. The carbon content within the whole cathodes differs, but the differences are rather small. Consequently, no drastic difference was apparent in the electrical conductivity of the p-CA cathodes. For f-CA, higher electrical conductivities are observed for the samples with lower sulfur content, although within the same order of magnitude. Again, it is assumed that the sulfur is hosted within the micro and mesoporous structure of the CA. In contrast to that, a lower electrical conductivity is noticeable for the f-CA cathode containing 60% of sulfur within the composite. This phenomenon can be explained by two effects. The micro- and mesopore structure of the f-CA is not capable of hosting the entire sulfur content, leading to sulfur precipitation on the outer carbon surface, thus decreasing the electrical conductivity of the carbon. Additionally, the carbon content is rather low compared to the other f-CA samples. This corresponds to the lowest electrical conductivity, which may contribute to the reduced sulfur utilization. The other cathodes display electrical conductivities that are rather high compared to typical conductivities of LS-SSBs in the literature, where values between 10 and 50 mS cm^{-1} have been reported using similar cathode compositions [13, 16]. Comparing the values of the pure CAs with those of the entire cathode, a different trend was observed, as p-CA demonstrated a higher conductivity as powder, but lower conductivity in the cathode compared to f-CA. This can be explained by the different densities and particle sizes of the CAs (Table 1), affecting the cathode morphology, and leading to different electronically conducting pathways within the cathode. Furthermore, an increased sulfur ratio was present within the p-CA samples, accompanied by a lowered carbon content in the cathode composition. Consequently, it can be concluded that sufficient electronic conductivity is provided as the percolation limit of the cathodes is not reached. Notably, the differences in electrochemical performance cannot be explained by the electric conductivity. The ionic conductivity within the LS-SSB cathode is crucial as the transport of Li^+-ions towards the reactive sites has to be ensured. However, measuring ionic conductivities solely provides insights into the ionic conductivity throughout the entire cathode rather than at the reactive sites. In LS-SSBs the provision of Li^+-ions at the reactive sites as well as the kinetics of the sulfur conversion are considered the bottleneck in sulfur utilization. Thus, C-rate testing is a more sensible method to gain insights into kinetic limitations than of ionic conductivity measurements, as discussed in Section 2.2.1.

2.2.3 | FIB-SEM Imaging of LS-SSB Cathodes

Electrical conductivity measurements as well as C-rate testing could not explain the differences in electrochemical performance since p-CA showed higher C-rate dependency and lower electronic conductivity, yet demonstrated significantly higher sulfur utilization. It is known from previous work that the cathode morphology and compression behavior are key parameters [16]. A low porosity of the cathodes is desirable, as it reduces grain boundaries and en sures the contact between the cathode's components. Remaining porosity within the cathode acts as an insulator, inhibiting the transport of Li^+-ions and electrons towards the reactive sites. To gain insights into the compressibility of the cathode, focussed ion beam scanning electron microscopy (FIB-SEM) imaging was performed for the cathodes with the best electrochemical performance ($V_{micro-+mesopore} = V_{Li2S}$), after compression at 360 MPa (Figure 6). An inhomogeneous structure of both cathodes is observed. Agglomerates of carbon and SE particles are visible adjacent to single particles in both samples and both cathodes demonstrate cracks and remaining porosity between the particles. In the case of p-CA, dark particles are observed next to a grey matrix and brighter particles. Voids and interstices are visible at higher magnification, where a substructure consisting of darker and brighter areas is noticeable. Larger powder particles without a substrate are predominant in p-CA. In contrast, the FIB-SEM image of f-CA displays smaller powdered particles with a characteristic fine substructure on the nm-scale. These observations agree with the powdered particle sizes of the CAs, as discussed in Section 2.1, when f-CA displays significantly lower powdered particle sizes than p-CA. At higher magnification f-CA displays a high amount of voids in the proximity of particles or particle agglomerations, indicating that the f-CA cathode is less densified and maintains the intrinsic structure of the cathode's components. This is further supported by density measurements of the dry films, where p-CA exhibits a density of 1.39 g cm^{-3}, while f-CA shows a lower density of 1.26 g cm^{-3}, confirming that the f-CA cathode is less densified. These observations are consistent with the lower sulfur utilization, as the SE is less compressed and voids are present, presumably resulting in decreased transport pathways within the f-CA cathode, which is crucial to ensure efficient sulfur utilization. In contrast, the compressed p-CA cathode can be considered as over-densified leaving insufficient free volume to accommodate the expansion during sulfur conversion, thereby restricting sulfur accessibility in subsequent cycles and ultimately leading to capacity fading during long-term cycling.

The flexible behavior of f-CA leads to different compression behavior, and, as a result, a lower density of the cathode. However, the small powdered particle sizes of f-CA could potentially be used to ensure a close-packing of the LS-SSB cathodes, as they may fill the voids and interstices between the larger p-CA powdered particles and SE particles. Consequently, a mixture of both CAs as a carbon host for LS-SSB cathodes was investigated in this work.

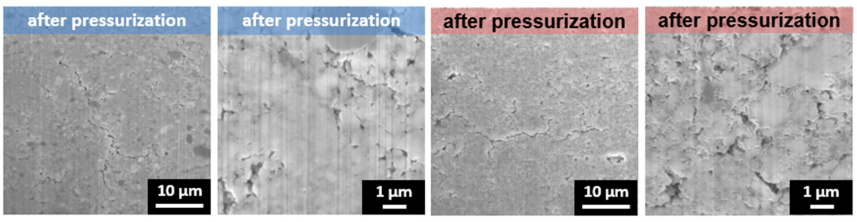

FIGURE 6 | FIB-SEM images of the p-CA (blue) and f-CA (pink) cathodes, after pressurization at 360 MPa.

25666223, 2026, 7, Downloaded from https://chemistry-europe.onlinelibrary.wiley.com/doi/10.1002/batt.70384 by Fraunhofer IRB, Wiley Online Library on [05/08/2026]. See the Terms and Conditions (https://onlinelibrary.wiley.com/terms-and-conditions) on Wiley Online Library for rules of use; OA articles are governed by the applicable Creative Commons License

2.3 | Electrochemical Characterization of LS-SSB Cathodes with a Combination of Two Different CAs

Given that each individual CA did not lead to a promising sulfur cathode performance, a combination of the f-CA-rich and p-CA-rich composites was generated. The aim was that the different particle sizes of p-CA and f-CA can contribute to an enhanced packing density, and, in turn, to higher compressive strain, where small powder particles of f-CA can be located between larger powdered particles of p-CA and fill some microscopic gaps. The increased packing density was presumed to decrease kinetic barriers caused by the remaining porosity within the cathode. The sulfur content was set to the lower sulfur contents (based on the Li_2S volume), since the best electrochemical performance was observed for this sulfur content in both carbons. Consequently, sulfur melt infiltrated p-CA and f-CA in two different ratios (p-CA:f-CA 80:20 and 70:30) were created. The detailed cathode composition is noted in Table 2 in Section 4.

The electrical conductivities of both composite materials are illustrated in Figure S2A, where the pure CAs were investigated as well as the melt-infiltrated carbons with the corresponding sulfur content. The conductivity curves of both composites are located between the values that were measured for pure aerogels, very close to pure p-CA. It is understood from the curves, that the properties of p-CA dominate in the composites and the influence of sulfur on conductivity is almost negligible. Surprisingly, when the compression behavior of the two composites is compared, it can be seen that they are dominated by f-CA.

In general, sulfur-infiltrated samples are slightly softer and/or more compressible than pure aerogels (Figure S2B). To the best of our knowledge, the influence of sulfur on electrical conductivity and compression has not yet been described in the literature. Sulfur acts like a lubricant between the carbon particles. Additionally, f-CA increases the softness of the composites. It is conceivable that this combination of different particle sizes leads to much better contact between the particles and thus increases conductivity. In another context, Celzard et al. emphasized in their study on the conductivity measurements of carbonaceous powders, similar results and pointed out the importance of the way the grains of carbonaceous powder are packed [40]. Ghislandi et al. also pointed out a strong effect of rearrangement and fragmentation of particles, their orientation, and packing density [41].

2.3.1 | Electrochemical Performance of LS-SSB Cathodes with a Combination of Two Different CAs

To achieve lower porosity of the LS-SSB cathodes, the two different ratio mixtures of p-CA and f-CA (80:20 and 70:30) were tested in LS-SSB as cathodes. The electrochemical performance of the mixed cathodes is displayed in Figure 7.

When comparing the voltage profiles at different C-rates (Figure 7A,B), the discharge plateaus remain more pronounced, even at the high C-rate of 0.5 C.

Correspondingly, the mixture of 80% p-CA with 20% f-CA (green) is characterized by an initial discharge capacity of 1260 mAh g_S^{-1}. In the subsequent cycles, a lowerdischarge

TABLE 2 | List of the cathode compositions tested in this work.

Cathode	Sulfur content in composite, %	Sulfur content in cathode, %	Carbon content in cathode, %	SE content in cathode, %
p-CA 53	53	26.5	23.5	50
p-CA 60	60	30	20	50
p-CA 65	65	32.5	17.5	50
f-CA 31	31	15.5	34.5	50
f-CA 44	44	22	28	50
f-CA 60	60	30	20	50
80:20-p:f	50	25	25	50
70:30-p:f	48	24	26	50

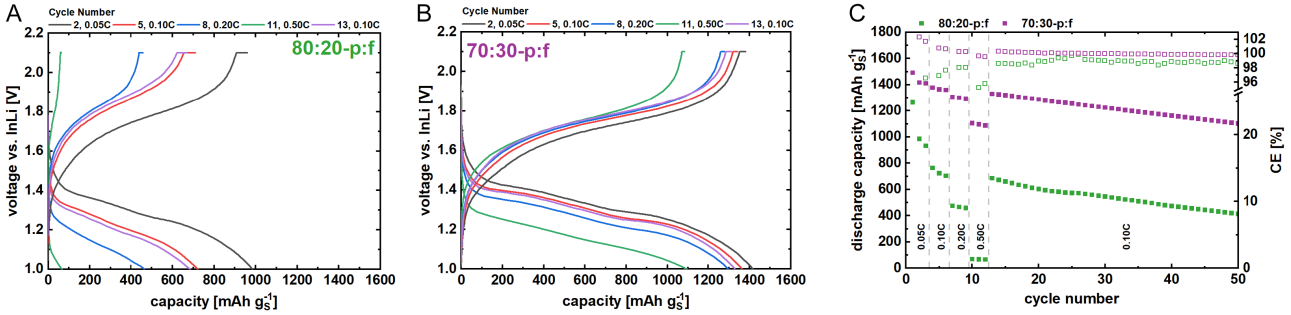

FIGURE 7 | Electrochemical performance of the mixed cathodes, (A) voltage profiles at different C-rates of 80:20-p:f, (B) voltage profiles at different C-rates of the 70:30-p:f blend, and (C) capacity retention during cycling.

25666223, 2026, 7, Downloaded from https://chemistry-europe.onlinelibrary.wiley.com/doi/10.1002/batt.70384 by Fraunhofer IRB, Wiley Online Library on [05/08/2026]. See the Terms and Conditions (https://onlinelibrary.wiley.com/terms-and-conditions) on Wiley Online Library for rules of use; OA articles are governed by the applicable Creative Commons License

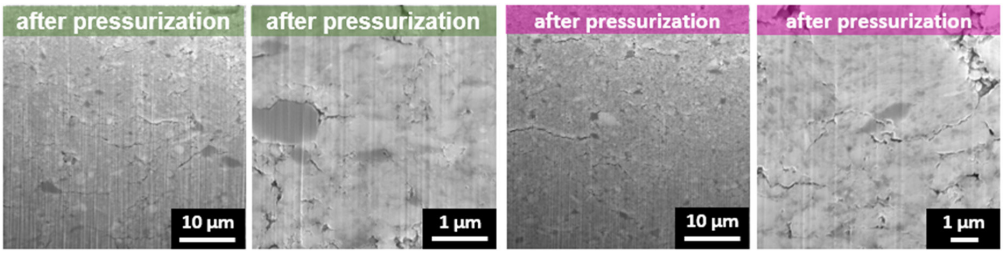

FIGURE 8 | FIB-SEM images of the 80:20-p:f (green) and the 70:30-p:f (purple) cathodes, after pressurization at 360 MPa.

capacity of approximately 950 mAh g_S^{-1} is detected at 0.05C. Increasing the C-rate results in a lower discharge capacity, where 720 mAh g_S^{-1} is obtained at 0.1C and 460 mAh g_S^{-1} is obtained at 0.2C. The discharge capacity is lowered drastically at the highest C-rate, demonstrating 70 mAh g_S^{-1} at 0.5°C. However, the discharge capacity is increased to 690 mAh g_S^{-1} in cycle 13. A linear capacity fade is observed during long-term cycling, resulting in 400 mAh g_S^{-1} after 50 cycles. The sulfur utilization of this cathode is lower compared to the pure p-CA cathode, but comparable to the electrochemical performance of the f-CA cathode. The second mixture that was tested contained a CA mixture of 70:30 (purple). It can be seen that the sulfur utilization is increased drastically, resulting in an initial discharge capacity of 1490 mAh g_S^{-1}. The discharge capacity is less significantly affected by increasing C-rates, resulting in 1300 mAh g_S^{-1} at 0.2C and 1100 mAh g_S^{-1} at the highest C-rate of 0.5C. High sulfur utilization is observed during long-term cycling, as well as a high CE close to 100%. Consequently, the capacity fade after 50 cycles is rather low, with 1100 mAh g_S^{-1} retained in the 50th cycle, corresponding to 80% of the capacity observed in cycle 5. The mixture of p-CA and f-CA in the ratio of 70:30 displays improved electrochemical performance, characterized by higher discharge capacities as well as a lower C-rate dependency. Compared to the pure p-CA, the CE of the mixed sample was further increased, improving the long-term stability and capacity retention during cycling. FIB-SEM imaging was performed after pressurization of the mixed cathode samples, as depicted in Figure 8. It was previously observed that the cathode solely consisting of f-CA (Figure 6, pink) is characterized by a finer substructure than p-CA, which was explained by the difference in compression behaviors and particle sizes. After compression, only a few distinct particles can be noticed, whilst a greyish matrix is present, as already observed in the p-CA cathode.

f-CA displayed lower powdered particle sizes and increased mechanical stability compared to p-CA, hence it was added to p-CA in lower ratio. Both cathodes demonstrate a morphology, which is more similar to the structure of the cathode prepared from pure p-CA, but with a reduced amount of voids or cracks. In the case of the 70:30 ratio, the smaller powder particles and the substrate appear more homogeneously blended whereas in the 80:20 ratio larger carbon domains are still noticeable in the gray matrix, and the overall appearance of the cathode is denser compared to the 70:30 composite. It is concluded that the addition of f-CA within the cathode sample leads to a lowered porosity of the cathode, as voids or cracks are filled with the small f-CA powdered particles, resulting in the observed structure. This interpretation is further supported by the density measurements of the dry films, where these two composites display very similar values of 1.21 g cm^{-3} for 70:30-p:f and 1.26 g cm^{-3} for 80:20-p:f. This suggests that f-CA fills in the gaps within the p-CA matrix more efficiently, enhancing the overall packing density. However, both composites still exhibit lower densities than pure p-CA53 (1.39 g cm^{-3}), indicating that they retain additional free volume. As highlighted by Um et al., the importance of uniform reaction distribution to mitigate diffusion-limited kinetics of lithium and sulfur reactions [42], it becomes clear that morphological nonuniformity in p-CA and the low packing density in f-CA lead to incomplete sulfur utilization and reduced electrochemical performance. Overall, the transport of both electrons and Li^+-ions within the cathode, with the combination of two different CAs was enhanced, resulting in more uniform morphology and higher packing density, compared to pure f-CA, which promotes more homogeneous reaction kinetics and enhanced overall electrode utilization.

This is also consistent with the findings of Oh et al. that discussed increasing packing density plays a crucial role in lowering kinetic barrier in sulfur conversion by providing more active site, thereby, shortening ion transport pathway and promoting faster electrochemical conversion [43].

3 | Conclusion

Two different CAs with varying porosity and mechanical stability have been investigated in this study as host matrix for LS-SSB cathodes. p-CA represented a brittle CA with mesopores, while f-CA is a flexible CA, predominantly characterized by macropores and lower micro- and mesopore volume. Additionally, p-CA was characterized by increased powder particle sizes compared to f-CA. Both CAs were investigated in LS-SSB cathodes using three different sulfur ratios each. It was demonstrated that the sulfur utilization is higher when using p-CA, realizing up to 1500 mAh g_S^{-1} at low C-rates. However, low CE and low reversibility of the sulfur conversion were observed during long-term cycling. In contrast to that, f-CA demonstrated lower sulfur utilization but enhanced reversibility during cycling. FIB-SEM imaging revealed different cathode morphologies, with f-CA exhibits a finer substructure, lowered porosity, and density. p-CA was characterized by voids and cracks after pressurization.

In order to decrease the undesired porosity/void formation within the p-CA cathode, a mixture of both CAs was used. It was presumed that the smaller particles of f-CA could fill the interstices between the p-CA particles, resulting in an increased packing density of the cathode while still retaining sufficient free volume to buffer the cathode expansion. It was successfully demonstrated that the mixture of p-CA and f-CA in a ratio 7:3 corresponding

25666223, 2026, 7, Downloaded from https://chemistry-europe.onlinelibrary.wiley.com/doi/10.1002/batt.70384 by Fraunhofer IRB, Wiley Online Library on [05/08/2026]. See the Terms and Conditions (https://onlinelibrary.wiley.com/terms-and-conditions) on Wiley Online Library for rules of use; OA articles are governed by the applicable Creative Commons License

to a threshold of 30% f-CA, leads to enhanced sulfur utilization, especially at increased C-rates, as well as long-term stability. High sulfur utilization above 1400 mAh g_S^{-1} was reached, accompanied with a high CE (>99.8%) throughout cycling. This work demonstrated the feasibility of CAs as host matrix in LS-SSBs reaching high sulfur utilization that approaches the promising and well-studied performance of the cost-intensive meso-porous carbon CNovel [16]. The combination of both aerogels led to an increased packing density of the cathode with better pathway for ion transfer through meso-/micro- and macropores network and to an enhanced electrochemical performance, and could be a principle methodology for other combinations of different carbons as host materials in sulfur/argyrodite based SSB cathodes. The adjustable porosity, mechanical properties, and particle sizes of the CAs represent a significant advantage, as they can be further tailored to meet specific application requirements and cost-efficiently up-scaled.

This study highlights, too, that the porosity of carbon materials is not the sole key performance indicator for the resulting sulfur utilization in cathodes; the flexibility of the carbons is crucial, too. In addition, mercury intrusion as method to analyze larger pores must be carefully considered when applied to flexible structures. Consequently, the final performance is revealed when the CAs are infiltrated with sulfur and implemented into a cathode. In future studies, the further validation of these results in pouch cells is be worth studying as this cell type offers more reliable results due to the homogeneous pressure distribution.

4 | Experimental Section

Classification of aerogels: For our study, we used two types of RF and carbonized them to CA. The first type, p-CA, is a brittle CA based on the work of Richard Pekala [44]. The second type, f-CA, is a flexible CA based on our own work [31].

4.1 | Synthesis

At room temperature, resorcinol (R) (98%, Aldrich) was dissolved in deionized water (W) with a molar ratio R/W of 0.038 for p-CA and 0.008 for f-CA and stirred at 150 rpm using a cross-magnetic stirring bar. Then, an aqueous solution of formaldehyde (F) and sodium carbonate (C) (Aldrich) was added to the stirred resorcinol solution. For p-CA, an aqueous solution of formaldehyde 24% w/w, not stabilized (VWR) with a molar ratio R/F of 0.74 and for f-CA, an aqueous solution of formaldehyde 37% w/w, stabilized with 10% methanol (Merck) with a molar ratio R/F of 0.5 was used. The molar ratio R/C was 250 for p-CA and 50 for f-CA. After 5 min of stirring, the pH of f-CA was adjusted to 5.4–5.6 by dropwise addition of 2 N nitric acid (Alfa Aesar). The pH value of p-CA was not changed. Stirring at room temperature was continued for 30 min for p-CA and 60 min for f-CA, followed by transferring the homogeneous transparent solution in a sealable polypropylene container to an oven at 60°C (Memmert GmbH, Germany). After 7 days of gelation and aging, the wet gel was cooled down to room temperature and transferred into an acetone bath (pure, technical grade, Th. Geyer) to remove residual reagents and exchange water by acetone being soluble in supercritical carbon dioxide. The acetone was refreshed 6 times within 3 days. Supercritical drying was performed with CO_2 (purity ≥99.995%, Praxair) in an autoclave of 60 L volume (Eurotechnica, Germany) at 60°C and 110 bar for about 21 h. The degassing rate was adjusted to 0.2 bar per minute.

4.2 | Carbonization

The carbonization was carried out in an electric furnace (KS-3- 80-Vac-Sonder, Linn High Therm, Germany) using nitrogen (purity ≥99.999%, Linde). The RF aerogels were placed in the furnace, purged three times with nitrogen, and heated to the carbonization temperature of 800°C for f-CA and 1000°C for p-CA. The temperature was kept constant for 5 h for f-CA and for 1 h for p-CA. The heating rate was adjusted to 2.5 K min^{-1} for f-CA and 5 K min^{-1} for p-CA, and the pressure was adjusted to 50 mbar. For f-CA, activation with CO_2 at 1000°C was followed for 3 h.

4.3 | Pulverization of Aerogels

For pulverization of the aerogel a shaker mill MM 400 (Retsch, Germany) was used. The milling process was conducted at a frequency of 30 Hz for 2 min for aerogels under dry conditions. Three hardened steel balls with a diameter of 15 mm were added into each milling jar.

4.4 | Nitrogen Physisorption

For physisorption experiments, the samples were degassed for 12 h at 200°C (SmartVacPrep, Micromeritics, Germany). The measurements of specific surface area, meso- and micropore size distribution, mesopore volume, and micropore volume were measured at 77 K via nitrogen adsorption–desorption isotherms (3Flex, Micromeritics, Germany). The calculations were based on BET/BJH/ DFT/t-plot methods. For t-plot and BJH, a carbon black STSA model and for the DFT method, an N_2-DFT model was used.

4.5 | Mercury Intrusion Porosimetry

For Hg-intrusion measurement of the sample, a MicroActive AutoPore V 9600 (Micromeritics, Unterschleißheim, Germany) equipped with a powder penetrometer was used. The analysis was conducted over a pressure range of 0.10–61,000 psia, corresponding to pore diameters from approximately 350 µm down to 6 nm. A mercury contact angle of 130° was applied at room temperature.

4.6 | Electrical Conductivity of Pure Carbon Aerogels

The electrical conductivity of powders was investigated using a resistivity measurement system (PD-51, Loresta GX, Mitsubishi Chemical Europe). The system is based on the 4-pin measuring method of surface resistance at constant pressures between 1 and 10 kN.

25666223, 2026, 7, Downloaded from https://chemistry-europe.onlinelibrary.wiley.com/doi/10.1002/batt.70384 by Fraunhofer IRB, Wiley Online Library on [05/08/2026]. See the Terms and Conditions (https://onlinelibrary.wiley.com/terms-and-conditions) on Wiley Online Library for rules of use; OA articles are governed by the applicable Creative Commons License

4.7 | Particle Size Distribution

The particle size distribution was determined using laser diffraction (LS13320, Beckman Coulter). A dry cell (Tornado Dry Powder Module) was used for the measurement.

4.8 | SEM and FIB-SEM

The microstructure of the aerogels was investigated using a scanning electron microscope (SEM) (Zeiss Merlin, Germany). Additionally, a SEM JSM-6060 (JEOL, Japan) was used for FIB-SEM analysis with an accelerating voltage of 10 kV.

4.9 | Cathode Preparation

The CAs were dried under vacuum at 200°C, overnight, whilst the sulfur (Sigma–Aldrich) was dried under vacuum at room temperature. Both materials were transferred into an argon-filled glove box and mixed in the desired weight ratios using a mortar. Afterwards, sulfur melt infiltration was performed at 155°C for 1 h under argon atmosphere. To obtain the LS-SSB cathodes, 150 mg of the prepared C-S-composites and 150 mg of SE (Li_6PS_5Cl, $D_{50} = 0.7\,\mu m$) were transferred into a ball mill jar (50 mL, 60 g ZrO_2 balls with 1 mm diameter) before mixing for 15 min at 300 rpm in a planetary ball mill (PM 100, Retsch GmbH). The obtained LS-SSB cathode material was transferred into a mortar and 0.5 wt% of polytetrafluoroethylene (PTFE) was added to prepare a dry-film cathode. The cathode material and PTFE were mixed in a mortar, applying gentle pressure (shear forces) at room temperature, before continuing the process at 100°C until a cathode flake was obtained. The flake was subsequently rolled at 80°C and punched to 11 mm diameter, realizing a loading of 1.5 $mg_S\ cm^{-2}$ (2.4 mAh cm^{-2}).

4.10 | All-Solid-State Battery (ASSBs) Cell Assembly

The anode was prepared by stomping 100 µm indium foil and 50 µm lithium foil to a diameter of 13 mm. Both foils were placed on the bottom current collector. Afterwards, 150 mg of SE (Li_6PS_5Cl, $D_{50} = 3.2\,\mu m$) was added and spread evenly using a spatula before pressurizing with a torque wrench at 3.5 Nm (20 MPa). The as-prepared cathodes were placed on top of the SE-layer before adding the upper current collector. The cell stack was pressurized at 360 MPa for 30 s using a hydraulic press. A torque wrench was used to apply external pressure of 3.5 Nm (20 MPa) during cycling.

4.11 | Galvanostatic Cycling

Galvanostatic cycling was carried out at a battery tester CTS-Lab (BaSyTec, Germany) at constant temperature of 25°C. After 5 h of resting, a rate performance test was performed. After symmetric cycles at 0.05 C, 3 cycles of rising C-rates during discharge have been performed (0.1°C, 0.2°C, and 0.5°C), whilst the charging current was kept constant at 0.1°C. The cells were cycled in a voltage range between 1.0 and 2.1 V versus InLi, where a CV-step was added during charging. 40 cycles at 0.1°C were added after rate test.

4.12 | Conductivity Measurements of Dry-Film Cathode

To measure the electronic conductivities of the LS-SSB cathodes, dry-film cathodes were prepared with 100 µm thickness and stomped out to a diameter of 13 mm. The dry films were placed within the lab-scale cell and pressurized at 360 MPa before applying constant pressure using a torque of 3.5 Nm (20 MPa). Direct current internal resistance measurement was carried out using a VSP-300 (Biologic, France). After a resting step of 30 min, a defined current of 100, −100, 200, −200, 240, and -240 mA was applied for 10 s. The resistance of the cathodes was calculated using Ohm's law ($R = U/I$). The thickness of the cathodes was measured afterwards to calculate specific electronic conductivity ($\sigma = L/(R \cdot A)$).

Acknowledgments

This research and development results are funded by the German Federal Ministry of Research, Technology, and Space (BMFTR, formerly BMBF) within the AReLiS-3 project (03XP0595).

Open Access funding enabled and organized by Projekt DEAL.

Funding

This study was supported by the Federal Ministry of Research, Technology and Space (BMFTR) (Funding Code: 03XP0595).

Conflicts of Interest

The authors declare no conflicts of interest.

Data Availability Statement

The data that support the findings of this study are available from the corresponding author upon reasonable request.

References

1. F. M. N. U. Khan, M. G. Rasul, A. Sayem, and N. K. Mandal, "Design and Optimization of Lithium-Ion Battery as an Efficient Energy Storage Device for Electric Vehicles: A Comprehensive Review," *Journal of Energy Storage* 71 (2023): 108033.

2. M. Sajjad, J. Zhang, S. Zhang, J. Zhou, Z. Mao, Z. Chen, Long-Life Lead-Carbon Batteries for Stationary Energy Storage Applications, *The Chemical Record* 2024, 24, e202300315.

3. M. R. Al Khazraji, J. Wang, and S. Wei, "Recent Progress of Anode Protection in Li–S Batteries," *Energy Technology* 11 (2023): 2200944.

4. T. Wang, J. He, Z. Zhu, et al., "Regulating Lithium Polysulfides for Advanced Lithium-Sulfur Batteries," *Advanced Materials (deerfield Beach, Fla.)* 35 (2023): e2303520.

5. S. J. Rettig and J. Trotter, "Refinement of the Structure of Orthorhombic Sulfur," *Acta Crystallographica Section C Crystal Structure Communications* 43 (1987): 2260–2262.

6. T. Hakari, Y. Sato, S. Yoshimi, A. Hayashi, and M. Tatsumisago, "Favorable Carbon Conductive Additives in Li 3 PS. 4 Composite Positive

25666223, 2026, 7, Downloaded from https://chemistry-europe.onlinelibrary.wiley.com/doi/10.1002/batt.70384 by Fraunhofer IRB, Wiley Online Library on [05/08/2026]. See the Terms and Conditions (https://onlinelibrary.wiley.com/terms-and-conditions) on Wiley Online Library for rules of use; OA articles are governed by the applicable Creative Commons License

Electrode Prepared by Ball-Milling for All-Solid-State Lithium Batteries," *Journal of the Electrochemical Society* 164 (2017): A2804–A2811.

7. Y. Guo, Q. Niu, F. Pei, et al., "Interface Engineering toward Stable Lithium–sulfur Batteries," *Energy & Environmental Science* 17 (2024): 1330–1367.

8. S. Dörfler, H. Althues, P. Härtel, T. Abendroth, B. Schumm, and S. Kaskel, "Challenges and Key Parameters of Lithium-Sulfur Batteries on Pouch Cell Level," *Joule* 4 (2020): 539–554.

9. S. Bandyopadhyay and B. Nandan, "A Review on Design of Cathode, Anode and Solid Electrolyte for True All-Solid-State Lithium Sulfur Batteries," *Materials Today Energy* 31 (2023): 101201.

10. P. Jiang, H. Zhou, S. Song, et al., "A Composite Cathode with a Three-Dimensional Ion/Electron-Conducting Structure for All-Solid-State Lithium–sulfur Batteries," *Communications Materials*. (2024): 5.

11. S. Kinoshita, K. Okuda, N. Machida, M. Naito, and T. Sigematsu, "All-Solid-State Lithium Battery with Sulfur/Carbon Composites as Positive Electrode Materials," *Solid State Ionics* 256 (2014): 97–102.

12. L. Froboese, J. F. van der Sichel, T. Loellhoeffel, L. Helmers, and A. Kwade, "Effect of Microstructure on the Ionic Conductivity of an All Solid-State Battery Electrode," *Journal of the Electrochemical Society* 166 (2019): A318–A328.

13. G. F. Dewald, S. Ohno, J. G. C. Hering, J. Janek, and W. G. Zeier, "Analysis of Charge Carrier Transport Toward Optimized Cathode Composites for All-Solid-State Li–S Batteries," *Batteries Supercaps* 4 (2021): 183–194.

14. A. Sakuda, Y. Sato, A. Hayashi, and M. Tatsumisago, "Sulfur-Based Composite Electrode with Interconnected Mesoporous Carbon for All-Solid-State Lithium–Sulfur Batteries," *Energy Technology* 7 (2019), https://doi.org/10.1002/ente.201900077.

15. R. Bradbury, G. F. Dewald, M. A. Kraft, et al., "Visualizing Reaction Fronts and Transport Limitations in Solid-State Li–S Batteries via Operando Neutron Imaging," *Advanced Energy Materials* 13 (2023), https://doi.org/10.1002/aenm.202203426.

16. M. Fiedler, M. A. Lange, F. Hippauf, et al., "The Role of Nanoporous Carbon Materials for Thiophosphate-Based All Solid State Lithium Sulfur Battery Performance," *Carbon* 227 (2024): 119252.

17. T. Ando, Y. Sato, T. Matsuyama, A. Sakuda, M. Tatsumisago, and A. Hayashi, "High-Rate Operation of Sulfur/Mesoporous Activated Carbon Composite Electrode for All-Solid-State Lithium-Sulfur Batteries," *Journal of the Ceramic Society of Japan* 128 (2020): 233–237.

18. A. F. Holleman, *Grundlagen Und Hauptgruppenelemente* (De Gruyter: Berlin/Boston, 2016, 103th

19. S. Wang, Y. Zhang, X. Zhang, et al., "High-Conductivity Argyrodite Li6PS5Cl Solid Electrolytes Prepared via Optimized Sintering Processes for All-Solid-State Lithium-Sulfur Batteries," *ACS Applied Materials & Interfaces*. (2018

20. M. Yamamoto, S. Goto, R. Tang, et al., "Nano-Confinement of Insulating Sulfur in the Cathode Composite of All-Solid-State Li–S Batteries Using Flexible Carbon Materials with Large Pore Volumes," *ACS Applied Materials & Interfaces* 13 (2021): 38613–38622.

21. X. Zhu, L. Wang, Z. Bai, J. Lu, and T. Wu, "Sulfide-Based All-Solid-State Lithium-Sulfur Batteries: Challenges and Perspectives," *Nano-Micro Letters* 15 (2023): 75.

22. H. Guo, J. Li, M. Burton, et al., "High-Entropy Sulfide Argyrodite Electrolytes for All-Solid-State Lithium-Sulfur Batteries," *Cell Reports Physical Science* 5 (2024): 102228.

23. J. Zhou, M. L. Holekevi Chandrappa, S. Tan, et al., "Healable and Conductive Sulfur Iodide for Solid-State Li-S Batteries," *Nature* 627 (2024): 301–305.

24. Y. Gao, D. Liu, Y. Zhao, et al., "Insights into Carbon-Based Aerogels Toward High-Performance Lithium–Sulfur Batteries: A Review of Strategies for Sulfur Incorporation Within Carbon Aerogel Frameworks," *Gels (basel, Switzerland)* 11 (2025): 516, https://doi.org/10.3390/gels11070516.

25. M. Nojabaee, B. Sievert, M. Schwan, et al., "Ultramicroporous Carbon Aerogels Encapsulating Sulfur as the Cathode for Lithium–sulfur Batteries," *Journal of Materials Chemistry A*. (2021): 6508.

26. M. Liu, Z. Yang, H. Sun, et al., "A Hybrid Carbon Aerogel with Both Aligned and Interconnected Pores as Interlayer for High-Performance Lithium–sulfur Batteries," *Nano Research* 9 (2016): 3735–3746, https://doi.org/10.1007/s12274-016-1244-1.

27. S. Zhu, L. Gong, Y. Pan, et al., "Coral-Like Interconnected Carbon Aerogel Modified Separator for Advanced Lithium-Sulfur Batteries," *Electrochimica Acta* 354 (2020): 136637, https://doi.org/10.1016/j.electacta.2020.136637.

28. A. Rege, M. Schwan, L. Chernova, M. Hillgärtner, M. Itskov, and B. Milow, "Microstructural and Mechanical Characterization of Carbon Aerogels: An in-Situ and Digital Image Correlation-Based Study," *Journal of Non-Crystalline Solids* 529 (2020): 119568, https://doi.org/10.1016/j.jnoncrysol.2019.119568.

29. M. Schwan, J. Schettler, F. M. Badaczewski, C. Heinrich, B. M. Smarsly, and B. Milow, "The Effect of Pulverization Methods on the Microstructure of Stiff, Ductile, and Flexible Carbon Aerogels," *Journal of Materials Science* 55 (2020): 5861–5879, https://doi.org/10.1007/s10853-020-04397-w.

30. R. W. Pekala, Alviso, "Carbon Aerogels and Xerogels," *C.T. Carbon Aerogels and Xerogels. MRS Online Proceedings Library* 270, no. 1 (1992): 3–14. https://doi.org/10.1557/PROC-270-3.

31. M. Schwan and Ratke, "Flexible Carbon Aerogels," *L. Flexible Carbon Aerogels. C* 2 (2016): 22, https://doi.org/10.3390/c2030022.

32. M. A. Aegerter, N. Leventis, M. M. Koebel, (Eds.) *Aerogels Handbook*, (Springer, 2011), ISBN 978-1-4419-7477-8, https://doi.org/10.1007/978-1-4419-7589-8.

33. M. Thommes, K. Kaneko, A. V. Neimark, et al., "Physisorption of Gases, with Special Reference to the Evaluation of Surface Area and Pore Size Distribution (IUPAC Technical Report)," *Pure and Applied Chemistry* 87 (2015): 1051–1069, https://doi.org/10.1515/pac-2014-1117.

34. L. Esquivias and N.de La Rosa-Fox, "Mercury Porosimetry Applied to Sono-Aerogels," *Journal of Sol-Gel Science and Technology* 26 (2003): 651–655, https://doi.org/10.1023/A:1020752911418.

35. G. Jiang, M. Fan, X. Shen, H. Gordon Harris, and S. D. Kenarsari, "The Buckling Deformation and Mechanical Properties of Aerogels Prepared with Polyethoxydisiloxane," *Microporous and Mesoporous Materials* 202 (2015): 183–188, https://doi.org/10.1016/j.micromeso.2014.09.050.

36. M. Fiedler, S. Cangaz, F. Hippauf, et al., "Mechanistic Insights into the Cycling Behavior of Sulfur Dry-Film Cathodes," *Advanced Sustainable Systems* 7 (2023): 2200439.

37. K.-J. Euler, "The Conductivity of Compressed Powders. A Review," *Journal of Power Sources* 3 (1978): 117–136, https://doi.org/10.1016/0378-7753(78)80011-1.

38. X. Lu, O. Nilsson, J. Fricke, and R. W. Pekala, "Thermal and Electrical Conductivity of Monolithic Carbon Aerogels," *Journal of Applied Physics* 73 (1993): 581–584, https://doi.org/10.1063/1.353367.

39. J. Kröner, D. Platzer, B. Milow, and M. Schwan, "Electrical Conductivity of Monolithic and Powdered Carbon Aerogels and Their Composites," *Materials Advances* 5 (2024): 8042–8052, https://doi.org/10.1039/D4MA00678J.

40. A. Celzard, J. F. Marêché, F. Payot, and G. Furdin, "Electrical Conductivity of Carbonaceous Powders," *Carbon* 40 (2002): 2801–2815, https://doi.org/10.1016/S0008-6223(02)00196-3.

41. M. Ghislandi, E. Tkalya, B. Marinho, C. E. Koning, and G.de With, "Electrical Conductivities of Carbon Powder Nanofillers and Their

25666223, 2026, 7, Downloaded from https://chemistry-europe.onlinelibrary.wiley.com/doi/10.1002/batt.70384 by Fraunhofer IRB, Wiley Online Library on [05/08/2026]. See the Terms and Conditions (https://onlinelibrary.wiley.com/terms-and-conditions) on Wiley Online Library for rules of use; OA articles are governed by the applicable Creative Commons License

Latex-Based Polymer Composites," *Composites Part A: Applied Science and Manufacturing* 53 (2013): 145–151, https://doi.org/10.1016/j.compositesa.2013.06.008.

42. K. Um, C. Jung, H. Nam, H. Lee, S. Yeom, and J. H. Moon, "Janus Architecture Host Electrode for Mitigating Lithium-Ion Polarization in High-Energy-Density Li–S Full Cells," *Energy & Environmental Science* 17 (2024): 9112–9121, https://doi.org/10.1039/D4EE02297A.

43. K. Oh, H. Nam, Y. Jang Chung, and J. Hyuk Moon, "Dry Carbothermal Reaction-Enabled Ultra-Dense Nanoparticle Coatings for High-Performance Li-S Batteries," *Chemical Engineering Journal* 499 (2024): 156229, https://doi.org/10.1016/j.cej.2024.156229.

44. R. W. Pekala, "Organic Aerogels from the Polycondensation of Resorcinol with Formaldehyde," *Journal of Materials Science* 24 (1989): 3221–3227, https://doi.org/10.1007/BF01139044.

Supporting Information

Additional supporting information can be found online in the Supporting Information section.

25666223, 2026, 7, Downloaded from https://chemistry-europe.onlinelibrary.wiley.com/doi/10.1002/batt.70384 by Fraunhofer IRB, Wiley Online Library on [05/08/2026]. See the Terms and Conditions (https://onlinelibrary.wiley.com/terms-and-conditions) on Wiley Online Library for rules of use; OA articles are governed by the applicable Creative Commons License